BAMS Article

Global Distributions of Atmospheric Turbulence Estimated Using Operational High Vertical-Resolution Radiosonde Data

Han-Chang Ko,[a] Hye-Yeong Chun,[a] Marvin A. Geller,[b] and Bruce Ingleby[c]

KEYWORDS: Dynamics; Turbulence; Radiosonde/ rawinsonde observations

ABSTRACT: Atmospheric turbulence plays a key role in the mixing of trace gases and diffusion of heat and momentum, as well as in aircraft operations. Although numerous observational turbulence studies have been conducted using campaign experiments and operational data, understanding the turbulence characteristics particularly in the free atmosphere remains challenging due to its small-scale, intermittent, and sporadic nature, along with limited observational data. To address this, turbulence in the free atmosphere is estimated herein based on the Thorpe method by using operational high vertical-resolution radiosonde data (HVRRD) with vertical resolutions of about 5 or 10 m across near-global regions, provided by the European Centre for Medium-Range Weather Forecasts (ECMWF) via the U.S. National Centers for Environmental Information (NCEI) for 6 years (October 2017–September 2023). Globally, turbulence is stronger in the troposphere than in the stratosphere, with maximum turbulence occurring about 6 km below the tropopause, followed by a sharp decrease above. Seasonal variations show strong tropospheric turbulence in summer and weak turbulence in winter for both hemispheres, while the stratosphere exhibits strong turbulence during spring. Regional analyses identify strong turbulence regions over the South Pacific and South Africa in the troposphere and over East Asia and South Africa in the stratosphere. Notably, turbulence information can be provided in regions and high altitudes that are not covered by commercial aircraft, suggesting its potential utility for both present and future high-altitude aircraft operations.

SIGNIFICANCE STATEMENT: The purpose of this study is to understand the characteristics of atmospheric turbulence in the free atmosphere, utilizing global high vertical-resolution radiosonde data (HVRRD) for recent 6 years (October 2017–September 2023). Our analysis shows that turbulence is stronger in the troposphere than in the stratosphere, with the maximum about 6 km below the tropopause. Regional analyses over 10 areas worldwide demonstrate the geographical characteristics in the troposphere and the stratosphere. This study will advance our understanding of atmospheric turbulence and help in development and validation of aviation turbulence forecasting systems for current and future high-altitude aircraft operations.

DOI: 10.1175/BAMS-D-23-0193.1
Corresponding author: Hye-Yeong Chun, chunhy@yonsei.ac.kr
Supplemental information related to this paper is available at the Journals Online website: https://doi.org/10.1175/BAMS-D-23-0193.s1.

Manuscript received 24 July 2023, in final form 19 September 2024, accepted 21 November 2024

AFFILIATIONS: [a] Department of Atmospheric Sciences, Yonsei University, Seoul, South Korea; [b] School of Marine and Atmospheric Sciences, Stony Brook University, State University of New York, Stony Brook, New York; [c] ECMWF, Reading, United Kingdom

1. Introduction

Atmospheric turbulence plays a vital role in the mixing of trace gases and diffusion of heat and momentum and is important for commercial airline operations due to its impact on aircraft passenger comfort and safety. Turbulence cannot be explicitly resolved in numerical weather prediction (NWP) models and is therefore parameterized in terms of turbulent kinetic energy (TKE) and diffusion (Janjić 2002; Shin and Hong 2011). In the aviation community, the NWP model output is used with turbulence indices representing favorable synoptic situations for generating turbulence or the breaking of gravity waves, to forecast the turbulence potential, rather than the turbulence itself. This assumes that potential turbulence regions can be identified based on the energy cascade from large- to small-scale phenomena (Sharman et al. 2006; Kim et al. 2011; Lee et al. 2020). These studies are susceptible to both the model and parameterization uncertainties, requiring validation via observational data. Particularly, in the development and validation of aviation turbulence forecasting systems utilizing multiple turbulence indices, global turbulence observations play a crucial role (Sharman et al. 2006; Sharman and Pearson 2017; Bechtold et al. 2021; D.-B. Lee et al. 2022; Shin et al. 2023).

For several decades, turbulence in the free atmosphere has been estimated using various data sources such as aircraft, radar, and radiosondes. While aircraft typically provides observations with a sufficient resolution and broad coverage when integrating data from multiple commercial flights over a long period, these observations are limited to the main flight routes (Nastrom and Gage 1985; Cho et al. 2003; Sharman et al. 2014; Dörnbrack et al. 2022). Radar offers temporally continuous data over specific sites, but requires significant costs and may not be feasible in many countries (Hocking 1983; Li et al. 2016). While operational radiosondes provide high vertical-resolution data up to about $z = 30$ km, previous studies have been confined to specific regions and relied on data provided by individual countries and national meteorological services (NMSs) (e.g., Clayson and Kantha 2008; Muhsin et al. 2016; Ko et al. 2019; Kohma et al. 2019; Zhang et al. 2019a,b; Lv et al. 2021). Although recent efforts have explored the use of small uncrewed aircraft systems (UASs) to address observation gaps (Pinto et al. 2021), current technical limitations restrict these to the lower atmosphere.

This lack of sufficient wide-scale, long-term observational data makes observing turbulence difficult, and even when turbulence is observed, understanding its characteristics is also a challenge due to its small-scale and intermittent nature. To facilitate reliable turbulence estimation globally, there should be three key observational requirements: (i) the data should have sufficiently high resolution, (ii) the coverage should be wide enough to include various regions, and (iii) the data should be provided routinely and operationally.

In this study, the global distribution of atmospheric turbulence in the free atmosphere is estimated using operational high vertical-resolution radiosonde data (HVRRD) provided by the European Centre for Medium-Range Weather Forecasts (ECMWF). The HVRRD provide in situ observations of basic atmospheric quantities such as air temperature, pressure,

horizontal wind, and humidity, along with the longitude, latitude, and altitude of each observation point from the global positioning system (GPS) following balloon drift. The HVRRD are routinely provided by operational radiosonde stations for synoptic weather observations with approximately 5- or 10-m vertical resolution, thereby enabling turbulence to be estimated quasi-globally and consistently without additional observation costs, although various quality control issues must be considered. Ingleby et al. (2016) discussed early progress in providing HVRRD to the NWP centers, and Pauley and Ingleby (2022) provided a recent update. These operational data have only recently become available to the atmospheric research community, and this study is believed to be the first to use this global HVRRD.

The aim of this study is to investigate the characteristics of global atmospheric turbulence in the troposphere and lower stratosphere by using operational HVRRD. In the following sections, the HVRRD is described. Then, the spatiotemporal distributions of turbulence are presented, along with regional analyses, followed by discussions on the potential applications to aviation turbulence. In this study, turbulence is estimated based on the Thorpe method (Thorpe 1977, 2005; Clayson and Kantha 2008), which has been used in numerous studies to estimate atmospheric turbulence in various geographic regions and periods (Nath et al. 2010; Muhsin et al. 2016; Ko et al. 2019; Kohma et al. 2019; Zhang et al. 2019a,b; Geller et al. 2021; Lv et al. 2021; Ko and Chun 2022; Ko et al. 2023). This method relies on identifying absolutely unstable layers that are assumed to be overturned by turbulent motion. Details of the Thorpe method are given in the appendix.

2. HVRRD

Operational radiosonde reports are exchanged internationally via the World Meteorological Organization (WMO) Information System (WIS). Different vertical resolutions exist at different stations and for different periods. This study utilized only radiosonde data with 1- and 2-s resolutions, which correspond to vertical resolutions of approximately 5 and 10 m, respectively. The ECMWF provides HVRRD from October 2014 to the present, with 460 stations providing at least 1 HVRRD profile each from October 2014 to September 2023. The data availability and monthly numbers of HVRRD stations are indicated in Fig. S1 in the online supplemental material. After mid-2017, the number of stations providing 1-s data significantly increased (Fig. S1b); therefore, the 6 years from October 2017 to September 2023 were selected for this study. Additionally, 2-s data have been available from approximately 100 stations since the end of 2015, which significantly increases the number of stations used in this study. Therefore, 2-s data were also utilized in this study. To ensure statistically robust results, only data from stations with 60 or more profiles in each season were used. The sensitivity to the selection of the minimum number of profiles was examined by changing the minimum numbers from 60 to 90 and 120. We found that the results with 90 and 120 profiles were almost identical to those with 60 (not shown).

A total of 332 stations and 947 319 profiles were used herein. As shown in Fig. 1, 187 (56%) of the stations provide 1-s data, 109 (33%) provide 2-s data, and 36 (11%) provide both 1- and 2-s data. Further, 248 (75%) of these stations are in the Northern Hemisphere (NH) and 84 (25%) are in the Southern Hemisphere (SH). Station information of these 332 stations is given in Table S1. Although China has 120 operational stations providing 1-s resolution data since 2011 (Guo et al. 2016), only lower-resolution data are exchanged internationally. The WMO Global Basic Observing Network (GBON, https://community.wmo.int/en/activity-areas/wigos/gbon) regulations will prompt higher resolution data exchange.

The radiosonde data used herein have undergone processing for radiation correction and smoothing (Ingleby et al. 2016). While several studies have documented the radiation corrections (e.g., von Rohden et al. 2022; S.-W. Lee et al. 2022), the smoothing process is proprietary to the

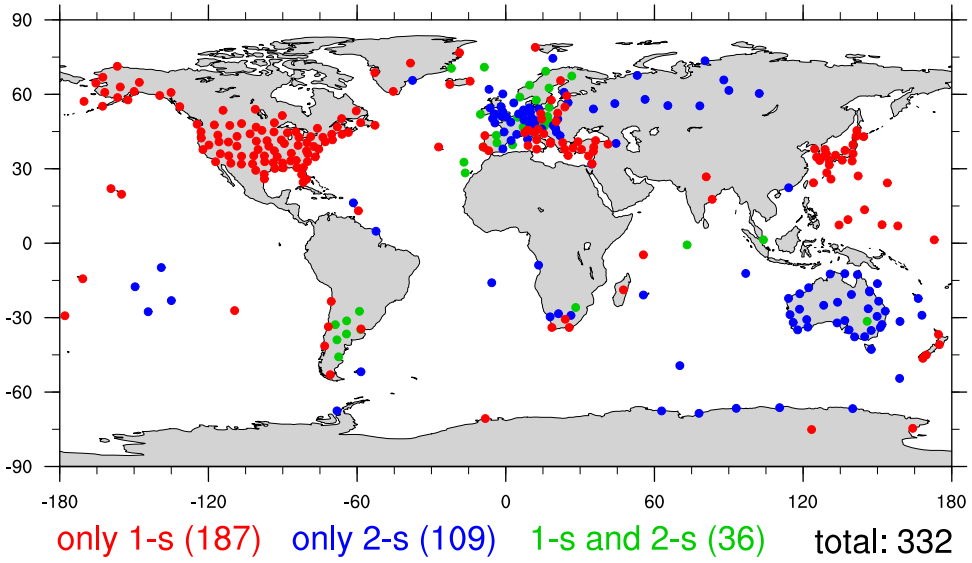

Fig. 1. Locations of radiosonde stations providing HVRRD with 60 or more profiles in each season for 6 years (October 2017–September 2023). Red, blue, and green indicate the stations that provide resolutions of only 1-s (187 stations), only 2-s (109 stations), and both 1- and 2-s (36 stations), respectively (332 stations in total).

instrument manufacturer and beyond public knowledge (Wang and Geller 2024, manuscript submitted to *J. Atmos. Oceanic Technol.*). Additionally, a total of 24 radiosonde instruments were used among the various stations (Fig. S2), each having its own errors and biases (e.g., Nash et al. 2011; Dirksen et al. 2014; Ingleby 2017; Pauley and Ingleby 2022). It remains uncertain how these errors and biases affect turbulence estimation. Meanwhile, Wang and Geller (2024, manuscript submitted to *J. Atmos. Oceanic Technol.*) indicated that temperature fluctuations are smaller in the processed data than in the raw data by up to a factor of 2 and vary depending on the radiosonde instruments. Hence, future studies are needed to assess the effects of the different instruments and processing methods on the turbulence estimation more rigorously.

3. Global distributions of turbulence

Histograms of $\log_{10}\varepsilon$ occurrence in the troposphere (from 3 km above the station height to the tropopause) and stratosphere (from the tropopause to 30 km) in the NH and SH are presented in Fig. 2, where the tropopause was calculated for each individual profile using the WMO (1957) definition of the first tropopause. Except for the SH stratosphere, where there were relatively few cases, a lognormal distribution is generally observed. Moreover, the mean and median of turbulence intensity are higher in the stratosphere than in the troposphere, as represented by mean $\log_{10}\varepsilon$ values of −3.47, −2.82, −3.39, and −2.84 $m^2\ s^{-3}$ in the NH troposphere, NH stratosphere, SH troposphere, and SH stratosphere, respectively, along with median values of −3.46, −2.85, −3.38, and −2.90 $m^2\ s^{-3}$, respectively. This contrasts with Ko et al. (2019), who reported that the mean ε was larger in the troposphere than in the stratosphere over the U.S. mainland during September 2012–August 2016. This is primarily because Ko et al. (2019) calculated the instrumental noise as a single value for the entire vertical range of the individual profile, whereas the instrumental noise was calculated as a variable quantity that generally increases with height herein. The larger instrumental noise in the stratosphere leads to a higher rejection rate of thin and weak turbulence layers (Wilson et al. 2011; Ko and Chun 2022), thereby contributing to a larger mean ε in the stratosphere. This is supported by the fact that the mean value of $\log_{10}\varepsilon$ is larger in the troposphere than in the stratosphere, in both the NH and the SH (not shown), when using a single value of instrumental noise as in Ko et al. (2019). Meanwhile, the number of occurrences of turbulence (n in Fig. 2) is significantly larger in the troposphere than in the stratosphere. This implies that turbulence is less likely

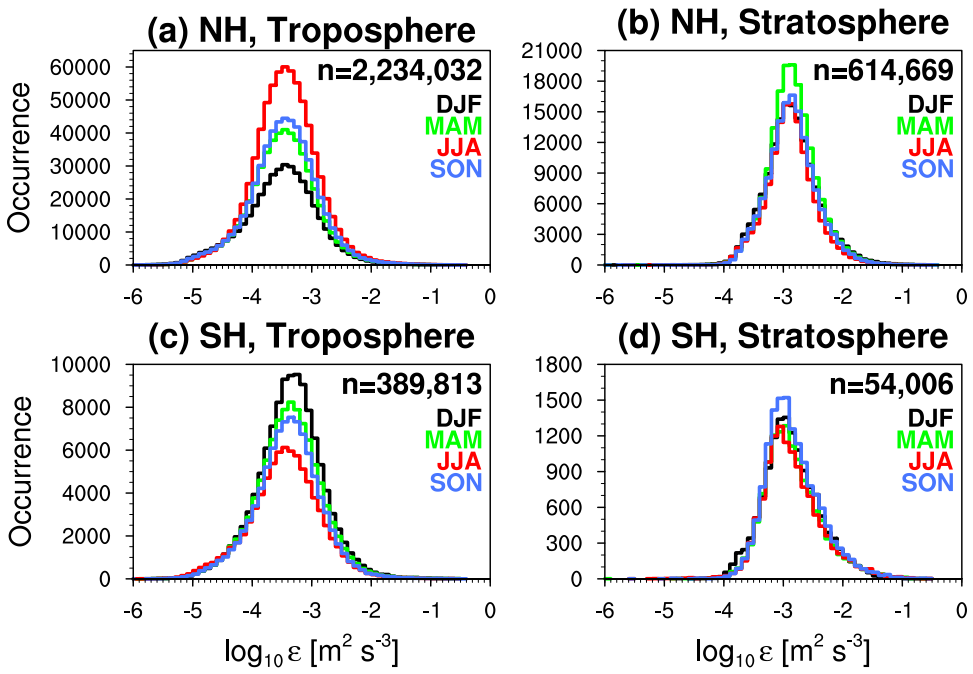

Fig. 2. Histograms of $\log_{10}\varepsilon$ occurrence in (a) the NH troposphere, (b) the NH stratosphere, (c) the SH troposphere, and (d) the SH stratosphere during October 2017–September 2023. The black, green, red, and blue lines represent the results for DJF, March–May (MAM), JJA, and September–November (SON), respectively, and "*n*" denotes the total occurrence number in each domain.

to occur in the stratosphere due to its relatively strong stability compared to the troposphere, but the intensity of turbulence overcoming this strong stability is larger than that in the troposphere. This is consistent with Zhang et al. (2022). Moreover, to assess the sensitivity of the statistics to the sample size, the mean and median $\log_{10}\varepsilon$ were also calculated by using 1000 and 10 000 random subsamples within each domain shown in Fig. 2. Furthermore, to avoid sampling bias, this procedure was performed 100 times, and the overall average of each statistic was reported as the result. The results in Table S2 indicate that the average values obtained using both 1000 and 10 000 subsamples are almost the same, and they are nearly the same as those shown in Fig. 2, thereby indicating that the statistics are robust, regardless of the varying sample size.

The seasonal variations in $\log_{10}\varepsilon$ are revealed by the different colors in Fig. 2. Maximum and minimum occurrences are observed during June–August (JJA) and December–February (DJF), respectively, in the NH troposphere (Fig. 2a), and during DJF and JJA, respectively, in the SH troposphere (Fig. 2c), thereby indicating the same seasonal variation. This is consistent with previous results obtained using HVRRD and the Thorpe method in various regions, including the United States (Geller et al. 2021; Ko and Chun 2022; Ko et al. 2023), India (Muhsin et al. 2016), and China (Lv et al. 2021). In the stratosphere, both the NH (Fig. 2b) and SH (Fig. 2d) show maximum turbulence occurrences during spring (MAM and SON, respectively), but the variation is less distinct in other seasons. This is partially consistent with Ko and Chun (2022), who showed that the occurrence numbers for $\log_{10}\varepsilon > -3$ m^2 s^{-3} are largest during spring. By contrast, when using HVRRD in China, Lv et al. (2021) found the largest occurrence frequency of turbulence in the stratosphere during summer. As noted above, the HVRRD used herein do not include the Chinese HVRRD, so this difference may be attributed to different geographical locations. It should also be noted that the distributions presented in Fig. 2 inherently reflect geographical biases due to the uneven distribution of radiosonde locations, as shown in Fig. 1. Regional analysis will be provided in the following sections.

The thickness of the turbulence layer (hereafter thickness) represents the vertical range where mixing of momentum and trace gases occurs. It is also considered a fundamental

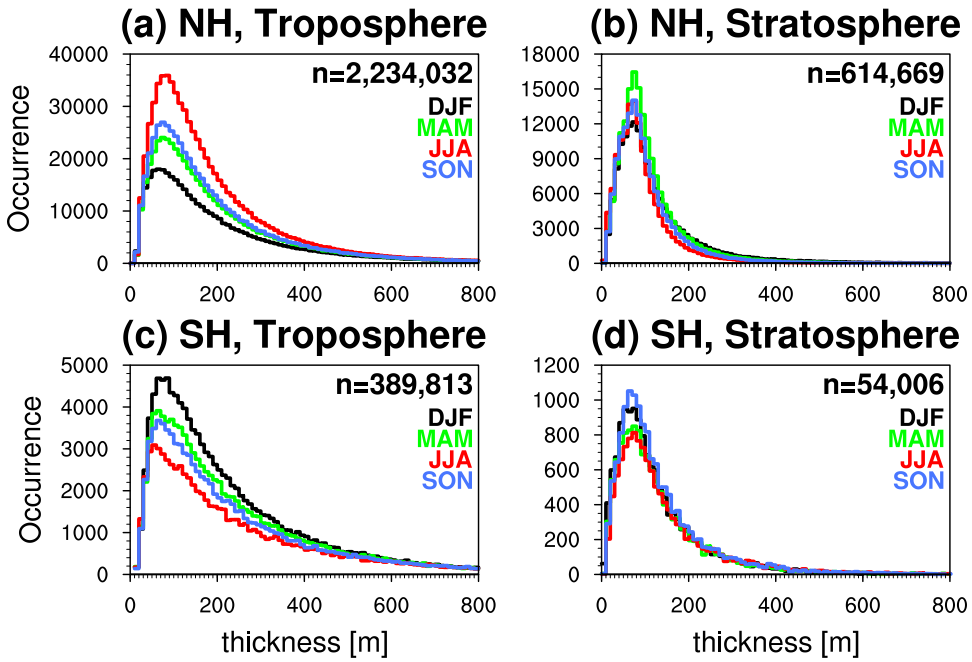

Fig. 3. Histograms of the thickness of the turbulence layer in (a) the NH troposphere, (b) the NH stratosphere, (c) the SH troposphere, and (d) the SH stratosphere during October 2017–September 2023.

parameter in turbulence modeling and parameterization (Dewan 1981; Osman et al. 2016; Muñoz-Esparza et al. 2020). The occurrence distributions of thickness are presented in Fig. 3. Here, thick layers of turbulence are generally more frequent in the troposphere than in the stratosphere, which is consistent with earlier works (Ko et al. 2019; Kohma et al. 2019; Geller et al. 2021; Ko and Chun 2022). Moreover, the seasonal variations in thickness are consistent with those observed in the $\log_{10}\varepsilon$ above: In the NH troposphere (Fig. 3a), thickness is more frequent and thicker during JJA, but less frequent and thinner during DJF. In the NH stratosphere (Fig. 3b), thickness is more frequent and thicker during MAM than in other seasons. In the SH, turbulence layer thickness in the troposphere (Fig. 3c) and stratosphere (Fig. 3d) exhibits same seasonal variations as in the NH.

The results in Fig. 3 demonstrate that the occurrence of thickness decreases sharply for thicknesses larger than the peak value (Luce et al. 2014; Bellenger et al. 2017; Wilson et al. 2018; Ko et al. 2019; Geller et al. 2021; Ko and Chun 2022). Osman et al. (2016) reported that turbulence diffusion is more strongly promoted by a small number of large thicknesses than a large number of low thicknesses. In Fig. 3, the median thickness values are 145, 80, 180, and 100 m in the NH troposphere, NH stratosphere, SH troposphere, and SH stratosphere, respectively, while the 95th percentiles are 600, 255, 760, and 360 m, respectively. This is consistent with the results of Bellenger et al. (2017), who reported peaks of thickness at 80–140 m over the tropical ocean. Notably, the statistics of thickness are larger in the SH than in the NH. As for the $\log_{10}\varepsilon$, the statistics of thickness in all four domains are nearly the same regardless of sample size (Table S3), although the similarity in the SH thickness is slightly less than that in the SH $\log_{10}\varepsilon$.

a. Horizontal distributions of turbulence. The above results indicate that the mean and median values of ε are larger in the stratosphere than in the troposphere, while the opposite is observed for the thickness value and occurrence (Figs. 2 and 3). The stronger average ε in the stratosphere is likely due to the smaller number of turbulence cases therein, thereby implying that, by itself, a nonzero average ε within a specific altitude bin does not properly represent the turbulence characteristics. To reconcile this situation, Ko and Chun (2022) proposed the effective ε (EE), which takes into account both the intensity (ε) and vertical range (thickness)

of turbulence. The EE is calculated using the formula $\mathrm{EE} = \sum(\varepsilon \times \mathrm{thickness})/Z\,(\mathrm{m^2\,s^{-3}})$, where Z is the layer depth of each altitude bin. In this study, Z is about 8.4 km for the troposphere that is defined from 3 km above the station height to the tropopause and is about 18.3 km for the stratosphere that is defined from the tropopause to z = 30 km for Figs. 4 and 5. On the other hand, a regular bin of 1 km is used for Fig. 6.

The global distributions of $\log_{10}$EE at each station during the study period are presented in Fig. 4. Generally, $\log_{10}$EE is much larger in the troposphere than in the stratosphere. In the troposphere, large values of $\log_{10}$EE occur over Türkiye, India, East Asia, South Pacific Islands, the lee side of the southern Andes, and South Africa, while small values appear at both poles. In the stratosphere, large values are observed over Türkiye, India, and East Asia, while small values appear in Northern Europe, Australia, and Antarctica. To the best of the author's knowledge, the present study is the first to provide observational evidence for maximum turbulence over Türkiye. Some studies have used global reanalysis data to indicate maximum turbulence indices over Türkiye and nearby. For example, Jaeger and Sprenger (2007) used 44 years of ERA40 data (ECMWF 40-yr reanalysis; Uppala et al. 2005) to reveal a summer

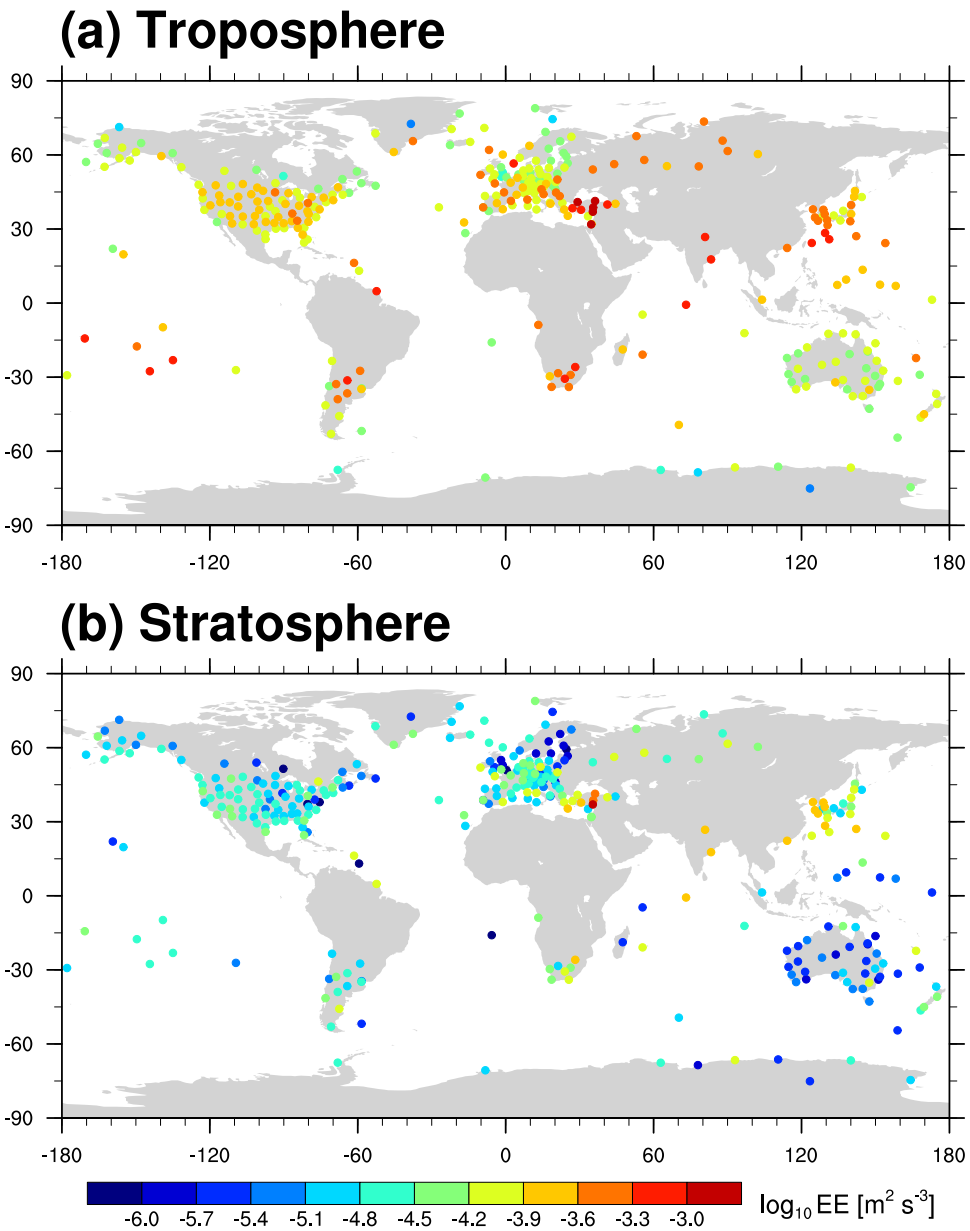

Fig. 4. The global distributions of $\log_{10}$EE at each station for October 2017–September 2023 in the (a) the troposphere and (b) the stratosphere.

maximum turbulence index near the tropopause over Türkiye, and Lee et al. (2023) used 41 years of ERA5 data (ECMWF reanalysis v5; Hersbach et al. 2020) to indicate a summer maximum turbulence index at 250 hPa over Mediterranean Europe. Within the U.S. mainland, this study identifies large values over the western Rocky Mountains and eastern Appalachian Mountains in the troposphere and along the edge of the U.S. mainland in the stratosphere (Fig. S3). This is consistent with Ko et al. (2019), who showed that local peaks in the troposphere can be associated with the mountain wave breaking and orographic convection, while those in the stratosphere may be related to the breaking of gravity waves generated from a relatively strong temperature gradient along the coastline.

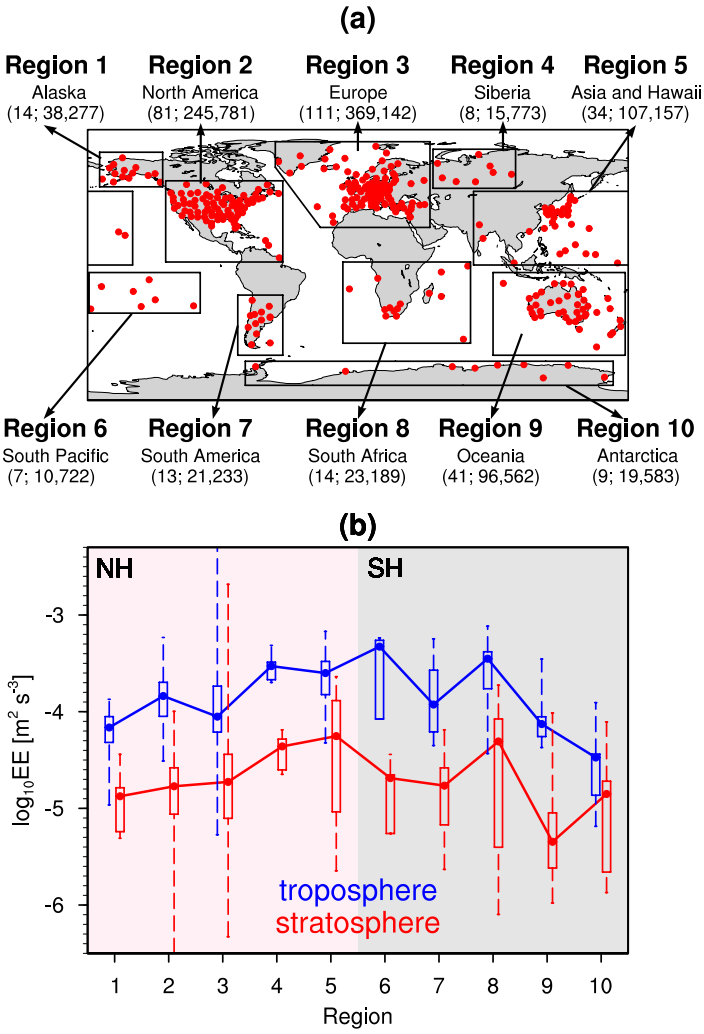

Fig. 5. (a) The division of radiosonde stations according to geographical region (regions 1–10), along with the numbers of stations and profiles, respectively, within each region for October 2017–September 2023. (b) Boxplots of $\log_{10}$EE in each region in the troposphere (blue) and stratosphere (red) for the 6-yr period. Lower and upper box boundaries represent the 25th and 75th percentiles, respectively, the dot inside the box is the median, and the dashed lines indicate the full range of values (minimum to maximum).

Different sources may contribute to turbulence depending on the region. In Türkiye and India, mountain waves due to high and complex terrain and their breaking can be sources of strong turbulence (Jaiswal et al. 2020; Rajput et al. 2022). In the lee side of the southern Andes, known as a hotspot for gravity waves (Hindley et al. 2019; Rapp et al. 2021), turbulence can be attributed to these waves. Climatologically, East Asia has the strongest jet stream over the globe (Koch et al. 2006), such that strong wind shear and the resultant Kelvin–Helmholtz instability (KHI), along with gravity wave activity induced by this jet stream, can contribute to turbulence (Jaeger and Sprenger 2007; Kim and Chun 2010, 2011; Lee and Chun 2018; Lee et al. 2023). In the South Pacific and South Africa, strong convection and associated convective gravity waves may contribute to strong turbulence (Kim et al. 2021).

The influence of the strength of the jet stream on the turbulence occurrence is examined. Here, the strength of the jet stream is evaluated based on the method by Koch et al. (2006). The turbulence occurrence frequency relative to the maximum jet location (Fig. S4) reveals that turbulence occurs more frequently under strong jet than weak jet conditions, which is somewhat expected. Interestingly, turbulence occurring is maximum about 2 km below the height of the jet maximum for both the strong and weak jet conditions, with larger frequency for the strong jet condition. When the influence of the strength of the jet stream on the turbulence occurrence frequency is further analyzed for each season (not shown), the turbulence

frequency is higher in strong jet streams than in weak jet streams across all seasons, with a maximum occurring below the height of the jet maximum, as shown in Fig. S4. Further analysis of the detailed generation mechanisms associated with the jet steam is needed in the future study.

Sources of turbulence include, but are not limited to, KHI generated by strong vertical wind shear in a thermally stable atmosphere, convective instability, and breaking gravity waves. However, differentiating between the sources of Thorpe-estimated turbulence is challenging. The Thorpe method exclusively estimates turbulence from θ overturning, and it is not straightforward to distinguish whether this θ overturning is generated by KHI or convective instability. Moreover, HVRRD may have limitations in investigating turbulence sources because it contains inherent turbulence effects, which cannot represent the background condition for generating the turbulence. For instance, Ko et al. (2019) reported almost no correlation between ε and vertical wind shear derived from HVRRD in the United States, likely due to mixing within each turbulence layer. Hence, Ko and Chun (2022) used the global reanalysis data with the highest currently available horizontal resolution, ERA5, to investigate the potential sources of turbulence in HVRRD estimates in the United States. They found that the low static stability and precipitation, along with the orographic gravity wave drag over the Rocky Mountains, are all strongly correlated with turbulence. Further, Zhang et al. (2022) reported a positive correlation between the turbulence frequency and the orographic gravity wave dissipation. Even without wave breaking, propagating gravity waves can modulate static stability and wind shear, leading to the onset of KHI and subsequent turbulence (Bellenger et al. 2017; Zhang et al. 2022; Woiwode et al. 2023). Further investigation into the generation mechanisms of Thorpe-estimated turbulence based on high-resolution numerical simulations is underway.

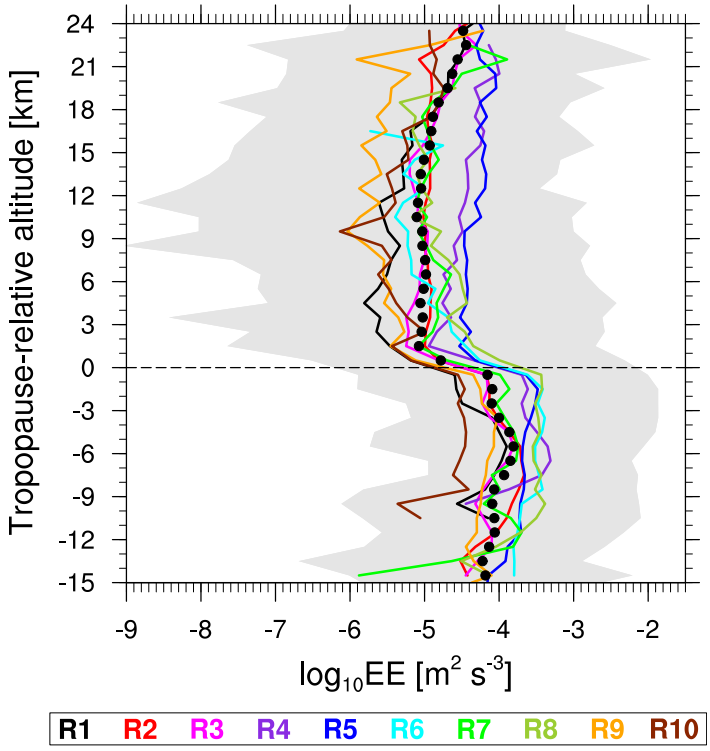

Fig. 6. The vertical distributions of $\log_{10}$EE for October 2017–September 2023 within each 1-km altitude bin with respect to the TP-relative altitude. The lines with colors represent the median of $\log_{10}$EE within each region shown in Fig. 5, and the black dots denote the median of $\log_{10}$EE of the total 332 stations. The gray shading indicates the full range of $\log_{10}$EE within each 1-km altitude bin.

The regional statistics of turbulence are further revealed by the regional distribution of $\log_{10}$EE in Fig. 5. In Fig. 5a, the globe is divided into 10 regions, with regions 1–5 in the NH and regions 6–10 in the SH, while boxplots of $\log_{10}$EE within each region are presented in Fig. 5b. The regions are selected by grouping geographically close areas, ensuring that all regions are not overlapped and that all radiosonde stations are included. As noted above, $\log_{10}$EE is generally larger in the troposphere than in the stratosphere. Thus, North America (region; R2), Europe (R3), and Asia and Hawaii (R5), which cover broad areas and various weather patterns, exhibit a wide range of $\log_{10}$EE values, whereas the regionally confined Alaska (R1) and Siberia (R4) exhibit a narrow range. Moreover, the range in the stratosphere is wider than that in the troposphere in most regions, thereby indicating higher

spatial variability of turbulence in the stratosphere. In terms of the median $\log_{10}$EE, global maxima occur in the South Pacific (R6) and Asia and Hawaii (R5) in the troposphere and stratosphere, respectively, while global minima occur in the Antarctica (R10) and Oceania (R9) in the troposphere and stratosphere, respectively. The large tropospheric values in the South Pacific (R6) and South Africa (R8) are consistent with the findings of Kim et al. (2021), who estimated near-cloud turbulence diagnostics based on convective gravity wave drag parameterization. Ko and Chun (2022) also found that the Thorpe-estimated turbulence is favorable in weak static stability and convective conditions.

b. Vertical distribution of turbulence. The vertical distribution of $\log_{10}$EE within each 1-km altitude bin is shown in Fig. 6. The results in Fig. 6 are based on the tropopause (TP)-relative altitude to consider the significant variations in TP height according to latitude and season (Birner 2006). In the following discussion, the TP-relative altitude is defined by z-z_{TP}, where z is the absolute altitude above mean sea level and z_{TP} is the TP height of an individual profile.

Log_{10}EE exhibits a significant difference between the troposphere and stratosphere, which is consistent with the findings in Figs. 4 and 5. The global median of $\log_{10}$EE (black dots) peaks at about TP-6 km, sharply decreases across the tropopause, remains relatively constant up to TP+12 km, and then increases again. The latter increase might be due to the increase in instrumental noise with height (Wilson et al. 2011), which leads to a higher rejection rate of thin turbulence layers at higher altitudes. Alternatively, Haack et al. (2014) suggested that the increase in turbulence with height may be due to the increasing kinematic viscosity. The present result is consistent with that of Clayson and Kantha (2008). Regionally, Siberia (R4), Asia and Hawaii (R5), South Pacific (R6), and South Africa (R8) exhibit higher values of median $\log_{10}$EE in the troposphere, indicating stronger turbulence in these regions. On the other hand, Antarctica (R10) shows lower values in the troposphere. In the stratosphere, Asia and Hawaii (R5) exhibits the highest values of $\log_{10}$EE, followed by Siberia (R4). Additionally, Alaska (R1), Oceania (R9), and Antarctica (R10) show lower values from the TP to TP+9 km. From TP+9 to TP+23 km, Oceania (R9) reveals the lowest values of $\log_{10}$EE. Moreover, the gray shading, representing the full range of $\log_{10}$EE of 332 stations, is wider in the stratosphere than in the troposphere. This indicates higher spatial variability of turbulence in the stratosphere, which is consistent with the findings in Fig. 5. For readers who may be interested in the individual values at each station, these values are provided in Fig. S5.

There are other definitions of tropopause height, such as the dynamical tropopause based on a potential vorticity iso-surface (2 potential vorticity units = 2×10^{-6} K m^2 s^{-1} kg^{-1}) and the potential temperature gradient tropopause (Tinney et al. 2022). In this study, analyses using both definitions were additionally conducted. Note that the dynamical tropopause height was retrieved from the ERA5 reanalysis at the nearest grid point from the radiosonde launch location, as the potential vorticity cannot be calculated using radiosonde data alone. The global-average height of the dynamical tropopause and the potential temperature gradient tropopause is 11 552 and 11 246 m, respectively, which is slightly less than that from the WMO tropopause of 11 731 m. It was found (not shown) that results shown in Figs. 2–6 using different definitions of the tropopause heights are nearly identical to those using the WMO tropopause definition.

4. Potential applications of HVRRD-derived turbulence in aviation turbulence

The results of this study have potential relevance to aviation turbulence, which causes injuries to passengers and crews, damage to aircrafts, and economic losses of millions of dollars (Sharman et al. 2006; Wolff and Sharman 2008). The accurate forecasting of aviation turbulence is crucial, and prediction systems are presently in operation (Sharman et al. 2006;

Sharman and Pearson 2017; Pearson and Sharman 2017; D.-B. Lee et al. 2022). To construct and validate such prediction systems, observational turbulence data are required. To date, only aircraft-based observations such as pilot reports (Sharman et al. 2006; Wolff and Sharman 2008; Kim and Chun 2011; Kim et al. 2011) and in situ flight data (Sharman et al. 2014; Kim et al. 2021; D.-B. Lee et al. 2022) have been used. However, aircraft provides data along flight paths only and avoids convective areas if possible, thus leading to sampling biases (Ko et al. 2023). By contrast, the HVRRD can provide turbulence information regardless of aircraft operations, thereby enhancing the observational data resources for aviation turbulence. For example, Ko et al. (2023) compared the HVRRD-based turbulence with in situ flight turbulence over the United States for a 6-yr period (2012–17). Given that radiosondes ascend more than 30 km on average, the HVRRD-derived turbulence can provide observations at the current cruising altitudes of commercial airlines along with the higher altitudes that future aircraft operations are expected to utilize [Federal Aviation Administration (FAA) 2020].

The global distributions of HVRRD-based turbulence counts within each 1° longitude × 1° latitude box within z = 5.4–18 km and 18–30 km are presented in Fig. 7. Here, two altitude ranges represent the class-A airspace used for commercial aircraft operations (https://www.faa.gov/air_traffic/publications/atpubs/aip_html/part2_enr_section_1.4.html) and the upper class-E airspace where operations have been limited due to the challenges in conventional fixed-wing aircraft in reduced air density (https://www.faa.gov/uas/advanced_operations/upper_class_etm), respectively. Figures 7a and 7c depict the total turbulence counts, while Figs. 7b and 7d show the distributions of moderate-or-greater (MOG) turbulence counts

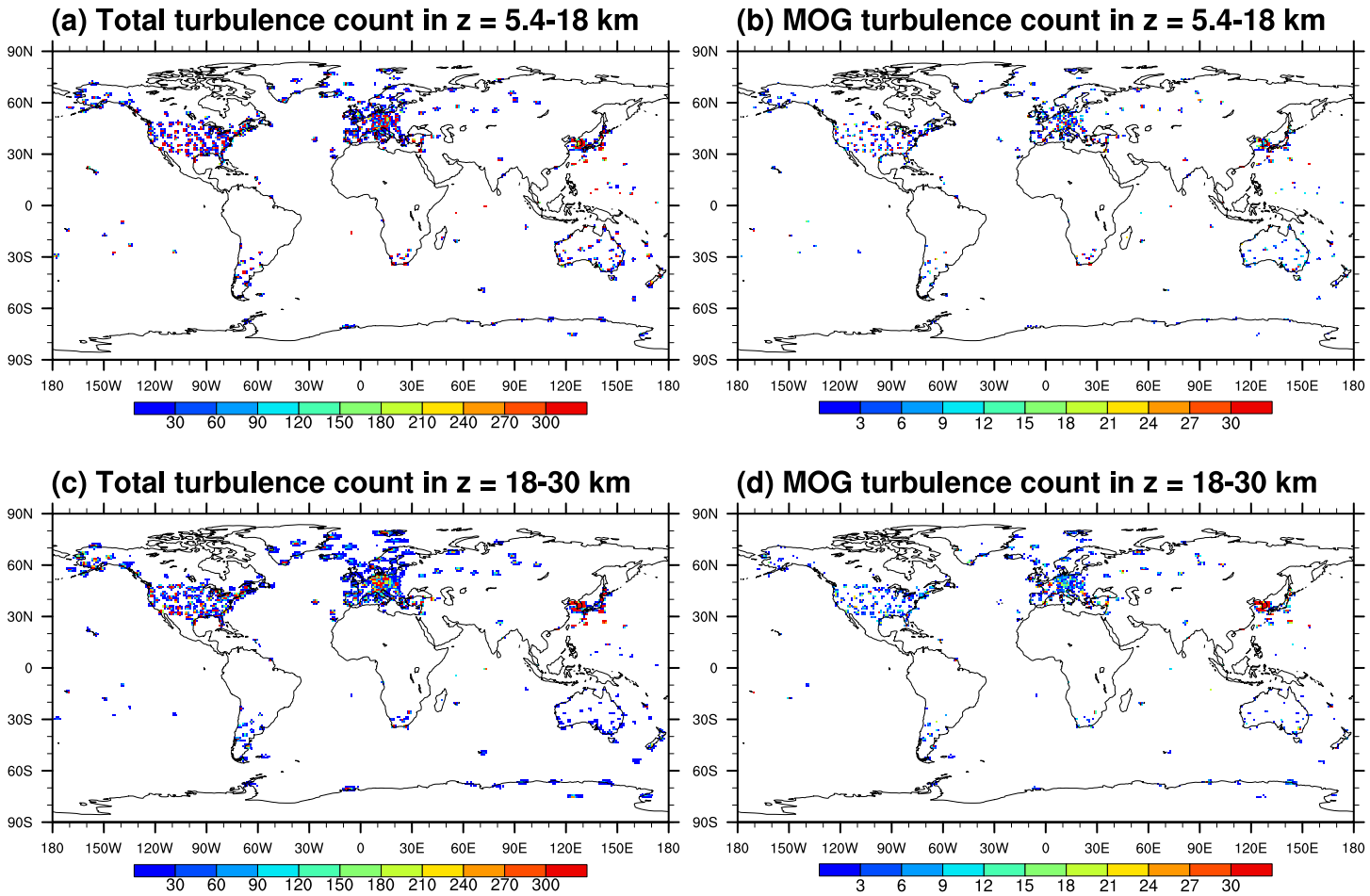

Fig. 7. (a),(c) The total turbulence count and (b),(d) the MOG turbulence count derived from HVRRD within each 1° longitude × 1° latitude box for October 2017–September 2023 at (a),(b) z = 5.4–18, and (c),(d) z = 18–30 km.

classified using the threshold $\varepsilon^{1/3} \geq 0.22\ m^{2/3}\ s^{-1}$ (Sharman and Pearson 2017). Here, turbulence counts are relatively large over the United States, Europe, East Asia, South America, South Africa, Australia, Greenland, Siberia, South Pacific, and Antarctica, as expected from Fig. 1. In total, 2 325 855 and 422 893 turbulence counts are detected within z = 5.4–18 km and 18–30 km, respectively. Among these, there are 19 435 (0.84%) and 14 388 (3.40%) counts of MOG turbulence within z = 5.4–18 km and 18–30 km, respectively. Although the counts are generally smaller in z = 18–30 km than in 5.4–18 km, except in East Asia near Korea and Japan, MOG turbulence is abundant, and turbulence is distributed more broadly due to increased drift from the station with height. Importantly, these turbulence observations can be used for turbulence nowcasting (Pearson and Sharman 2017). By utilizing these turbulence observations from HVRRD, the aviation industry can better predict and mitigate turbulence-related risks, thereby enhancing flight safety for both current and future high-altitude aircraft operations.

Acknowledgments. This research was supported by the Korea Meteorological Administration (KMA) Research and Development Program under Grant RS-2022-KM220410.

Data availability statement. All radiosonde data used in this study are openly available from the National Centers for Environmental Information (NCEI), available online at https://www.ncei.noaa.gov/data/ecmwf-global-upper-air-bufr/. Radiosonde data are decoded using ecCodes, available online at https://github.com/ecmwf/eccodes/. ERA5 reanalysis datasets are downloaded from the European Centre for Medium-Range Weather forecasts (ECMWF), available online at https://cds.climate.copernicus.eu/.

APPENDIX

Turbulence Estimation: Thorpe Method

The Thorpe method (Thorpe 1977, 2005; Clayson and Kantha 2008) is used to estimate turbulence in the free atmosphere. To understand how it works, first consider that potential temperature θ increases with height in the stable atmosphere. If θ overturning occurs (i.e., low θ in the upper level and high θ in the lower level), this is assumed to be accompanied by turbulent motions (Thorpe 2005). Because θ is a conserved quantity for adiabatic motions, the observed θ overturning can be sorted to a stably stratified profile by using a sorting algorithm. During this process, the individual vertical displacements of θ are defined as the Thorpe displacements (d). The thickness of the turbulence layer is then defined as the vertical range of successive nonzero values of d. Then, the root-mean-square d within each turbulence layer is defined as the Thorpe scale (L_T). Meanwhile, the Ozmidov scale (L_O) is defined by $L_O = (\varepsilon/N^3)^{1/2}$, where ε is the rate of turbulent kinetic energy dissipation and N is the Brunt–Väisälä frequency (Ozmidov 1965). Assuming a linear relationship between L_T and L_O, ε can be calculated as $\varepsilon = C_K L_T^2 N^3$, where C_K is the square of the linear coefficient between L_T and L_O. Note that one-third power of ε (EDR $\equiv \varepsilon^{1/3}$) is used as the standard metric of turbulence in aviation meteorology [International Civil Aviation Organization (ICAO) 2010].

Previous studies have shown that C_K varies depending on the source and development stage of the turbulence (e.g., Schneider et al. 2015; Scotti 2015; Fritts et al. 2016; Wang et al. 2019) and the altitude (Balsley et al. 2018; Kohma et al. 2019). It is difficult to distinguish the sources and development stages of turbulence because HVRRD inherently include turbulence effects (Ko et al. 2019). Nevertheless, C_K can be estimated from a comparison with other measurements or numerical simulations. For instance, Schneider et al. (2015) used the HVRRD and Leibniz Institute of Turbulence Observations in the Stratosphere (LITOS) data to show that individually determined C_K values vary by two orders of magnitude. Subsequently, Kohma et al. (2019) used ε values calculated using radar and HVRRD to show that C_K varies with height. Using direct numerical simulations (DNSs), Fritts et al. (2016) also found that C_K

varies by more than two orders of magnitude for individual turbulence events, but Wang et al. (2019) showed that C_K converges to a single value after averaging many profiles. Moreover, several studies have indicated general agreement between ε estimated using the Thorpe method and other measurements (Kantha and Hocking 2011; Li et al. 2016; Jaiswal et al. 2020). In particular, Kantha and Hocking (2011) and Li et al. (2016) showed a good agreement between the radar-estimated ε and the Thorpe-estimated ε when using $C_K = 1$. Therefore, it is assumed that $C_K = 1$ herein.

Before applying the Thorpe method, the same data processing as in Ko and Chun (2022) was applied, except that both the 1- and 2-s resolution HVRRD were used in this study and interpolated into 5- and 10-m intervals, respectively, whereas Ko and Chun (2022) exclusively used 1-s resolution HVRRD. Instrumental noise correction was performed via the method of Wilson et al. (2010, 2011), and moisture correction was performed according to Wilson et al. (2013). Details can be found in Ko and Chun (2022). Herein, turbulence was estimated exclusively in the free atmosphere, specifically 3 km above the station height, as the Thorpe method is valid above the assumed convective surface boundary layer (Thorpe 2005). During the visual check, several abnormally strong ε values were observed, likely due to erroneously strong vertical temperature gradients. Such gradients, whether positive or negative, induce strong artificial θ overturning and, hence, a strong ε. As it is difficult to set a threshold on the temperature gradient for HVRRD, turbulence cases with ε values of less than the 99.99th percentile (0.3195 $m^2 s^{-3}$) globally were permitted herein. This corresponds to the EDR ($=\varepsilon^{1/3}$) value of 0.68 $m^{2/3} s^{-1}$, which is twice the threshold of severe intensity 0.34 $m^{2/3} s^{-1}$ given by Sharman and Pearson (2017).

References

Balsley, B. B., D. A. Lawrence, D. C. Fritts, L. Wang, K. Wan, and J. Werne, 2018: Fine structure, instabilities, and turbulence in the lower atmosphere: High-resolution in situ slant-path measurements with the DataHawk UAV and comparisons with numerical modeling. *J. Atmos. Oceanic Technol.*, **35**, 619–642, https://doi.org/10.1175/JTECH-D-16-0037.1.

Bechtold, P., M. Bramberger, A. Dörnbrack, L. Isaksen, and M. Leutbecher, 2021: Experimenting with a clear air turbulence (CAT) index from the IFS. ECMWF Tech. Memo. 874, 15 pp., https://doi.org/10.21957/4L34TQLJM.

Bellenger, H., R. Wilson, J. L. Davison, J. P. Duvel, W. Xu, F. Lott, and M. Katsumata, 2017: Tropospheric turbulence over the tropical open ocean: Role of gravity waves. *J. Atmos. Sci.*, **74**, 1249–1271, https://doi.org/10.1175/JAS-D-16-0135.1.

Birner, T., 2006: Fine-scale structure of the extratropical tropopause region. *J. Geophys. Res.*, **111**, D04104, https://doi.org/10.1029/2005JD006301.

Cho, J. Y. N., R. E. Newell, B. E. Anderson, J. D. W. Barrick, and K. L. Thornhill, 2003: Characterizations of tropospheric turbulence and stability layers from aircraft observations. *J. Geophys. Res.*, **108**, 8784, https://doi.org/10.1029/2002JD002820.

Clayson, C. A., and L. Kantha, 2008: On turbulence and mixing in the free atmosphere inferred from high-resolution soundings. *J. Atmos. Oceanic Technol.*, **25**, 833–852, https://doi.org/10.1175/2007JTECHA992.1.

Dewan, E. M., 1981: Turbulent vertical transport due to thin intermittent mixing layers in the stratosphere and other stable fluids. *Science*, **211**, 1041–1042, https://doi.org/10.1126/science.211.4486.1041.

Dirksen, R. J., M. Sommer, F. J. Immler, D. F. Hurst, R. Kivi, and H. Vömel, 2014: Reference quality upper-air measurements: GRUAN data processing for the Vaisala RS92 radiosonde. *Atmos. Meas. Tech.*, **7**, 4463–4490, https://doi.org/10.5194/amt-7-4463-2014.

Dörnbrack, A., P. Bechtold, and U. Schumann, 2022: High-resolution aircraft observations of turbulence and waves in the free atmosphere and comparison with global model predictions. *J. Geophys. Res. Atmos.*, **127**, e2022JD036654, https://doi.org/10.1029/2022JD036654.

FAA, 2020: Upper Class E traffic management (ETM). Accessed 31 January 2024, https://www.faa.gov/uas/advanced_operations/upper_class_etm.

Fritts, D. C., L. Wang, M. A. Geller, D. A. Lawrence, J. Werne, and B. B. Balsley, 2016: Numerical modeling of multiscale dynamics at a high Reynolds number: Instabilities, turbulence, and an assessment of Ozmidov and Thorpe scales. *J. Atmos. Sci.*, **73**, 555–578, https://doi.org/10.1175/JAS-D-14-0343.1.

Geller, M. A., P. T. Love, and L. Wang, 2021: A climatology of unstable layers in the troposphere and lower stratosphere: Some early results. *Mon. Wea. Rev.*, **149**, 1233–1245, https://doi.org/10.1175/MWR-D-20-0276.1.

Guo, J., and Coauthors, 2016: The climatology of planetary boundary layer height in China derived from radiosonde and reanalysis data. *Atmos. Chem. Phys.*, **16**, 13 309–13 319, https://doi.org/10.5194/acp-16-13309-2016.

Haack, A., M. Gerding, and F. J. Lübken, 2014: Characteristics of stratospheric turbulent layers measured by LITOS and their relation to the Richardson number. *J. Geophys. Res. Atmos.*, **119**, 10 605–10 618, https://doi.org/10.1002/2013JD021008.

Hersbach, H., and Coauthors, 2020: The ERA5 global reanalysis. *Quart. J. Roy. Meteor. Soc.*, **146**, 1999–2049, https://doi.org/10.1002/qj.3803.

Hindley, N. P., C. J. Wright, N. D. Smith, L. Hoffmann, L. A. Holt, M. J. Alexander, T. Moffat-Griffin, and N. J. Mitchell, 2019: Gravity waves in the winter stratosphere over the Southern Ocean: High-resolution satellite observations and 3-D spectral analysis. *Atmos. Chem. Phys.*, **19**, 15 377–15 414, https://doi.org/10.5194/acp-19-15377-2019.

Hocking, W. K., 1983: On the extraction of atmospheric turbulence parameters from radar backscatter Doppler spectra—I. Theory. *J. Atmos. Terr. Phys.*, **45**, 89–102, https://doi.org/10.1016/S0021-9169(83)80013-0.

ICAO, 2010: Meteorological service for international air navigation. 206 pp., https://www.icao.int/airnavigation/IMP/Documents/Annex%203%20-%2075.pdf.

Ingleby, B., 2017: An assessment of different radiosonde types 2015/2016. ECMWF Tech. Memo. 807, 71 pp.

——, and Coauthors, 2016: Progress toward high-resolution, real-time radiosonde reports. *Bull. Amer. Meteor. Soc.*, **97**, 2149–2161, https://doi.org/10.1175/BAMS-D-15-00169.1.

Jaeger, E. B., and M. Sprenger, 2007: A Northern Hemispheric climatology of indices for clear air turbulence in the tropopause region derived from ERA40 reanalysis data. *J. Geophys. Res.*, **112**, D20106, https://doi.org/10.1029/2006JD008189.

Jaiswal, A., D. V. Phanikumar, S. Bhattacharjee, and M. Naja, 2020: Estimation of turbulence parameters using ARIES ST Radar and GPS radiosonde measurements: First results from the central Himalayan region. *Radio Sci.*, **55**, e2019RS006979, https://doi.org/10.1029/2019RS006979.

Janjić, Z. I., 2002: Nonsingular implementation of the Mellor–Yamada level 2.5 scheme in the NCEP Meso model. NCEP Office Note 437, 61 pp., https://www.emc.ncep.noaa.gov/officenotes/newernotes/on437.pdf.

Kantha, L., and W. Hocking, 2011: Dissipation rates of turbulence kinetic energy in the free atmosphere: MST radar and radiosondes. *J. Atmos. Sol.-Terr. Phys.*, **73**, 1043–1051, https://doi.org/10.1016/j.jastp.2010.11.024.

Kim, J.-H., and H.-Y. Chun, 2010: A numerical study of clear-air turbulence (CAT) encounters over South Korea on 2 April 2007. *J. Appl. Meteor. Climatol.*, **49**, 2381–2403, https://doi.org/10.1175/2010JAMC2449.1.

——, and ——, 2011: Statistics and possible sources of aviation turbulence over South Korea. *J. Appl. Meteor. Climatol.*, **50**, 311–324, https://doi.org/10.1175/2010JAMC2492.1.

——, ——, R. D. Sharman, and T. L. Keller, 2011: Evaluations of upper-level turbulence diagnostics performance using the Graphical Turbulence Guidance (GTG) system and pilot reports (PIREPs) over East Asia. *J. Appl. Meteor. Climatol.*, **50**, 1936–1951, https://doi.org/10.1175/JAMC-D-10-05017.1.

Kim, S.-H., H.-Y. Chun, D.-B. Lee, J.-H. Kim, and R. D. Sharman, 2021: Improving numerical weather prediction–based near-cloud aviation turbulence forecasts by diagnosing convective gravity wave breaking. *Wea. Forecasting*, **36**, 1735–1757, https://doi.org/10.1175/WAF-D-20-0213.1.

Ko, H.-C., and H.-Y. Chun, 2022: Potential sources of atmospheric turbulence estimated using the Thorpe method and operational radiosonde data in the United States. *Atmos. Res.*, **265**, 105891, https://doi.org/10.1016/j.atmosres.2021.105891.

——, ——, R. Wilson, and M. A. Geller, 2019: Characteristics of atmospheric turbulence retrieved from high vertical-resolution radiosonde data in the United States. *J. Geophys. Res. Atmos.*, **124**, 7553–7579, https://doi.org/10.1029/2019JD030287.

——, ——, R. D. Sharman, and J.-H. Kim, 2023: Comparison of eddy dissipation rate estimated from operational radiosonde and commercial aircraft observations in the United States. *J. Geophys. Res. Atmos.*, **128**, e2023JD039352, https://doi.org/10.1029/2023JD039352.

Koch, P., H. Wernli, and H. C. Davies, 2006: An event-based jet-stream climatology and typology. *Int. J. Climatol.*, **26**, 283–301, https://doi.org/10.1002/joc.1255.

Kohma, M., K. Sato, Y. Tomikawa, K. Nishimura, and T. Sato, 2019: Estimate of turbulent energy dissipation rate from the VHF radar and radiosonde observations in the Antarctic. *J. Geophys. Res. Atmos.*, **124**, 2976–2993, https://doi.org/10.1029/2018JD029521.

Lee, D.-B., and H.-Y. Chun, 2018: A numerical study of aviation turbulence encountered on 13 February 2013 over the Yellow Sea between China and the Korean Peninsula. *J. Appl. Meteor. Climatol.*, **57**, 1043–1060, https://doi.org/10.1175/JAMC-D-17-0247.1.

——, ——, and J.-H. Kim, 2020: Evaluation of multimodel-based ensemble forecasts for clear-air turbulence. *Wea. Forecasting*, **35**, 507–521, https://doi.org/10.1175/WAF-D-19-0155.1.

——, ——, S.-H. Kim, R. D. Sharman, and J.-H. Kim, 2022: Development and evaluation of global Korean aviation turbulence forecast systems based on an operational numerical weather prediction model and in situ flight turbulence

observation data. *Wea. Forecasting*, **37**, 371–392, https://doi.org/10.1175/WAF-D-21-0095.1.

Lee, J. H., J. Kim, R. D. Sharman, J. Kim, and S. Son, 2023: Climatology of clear-air turbulence in upper troposphere and lower stratosphere in the Northern Hemisphere using ERA5 reanalysis data. *J. Geophys. Res. Atmos.*, **128**, e2022JD037679, https://doi.org/10.1029/2022JD037679.

Lee, S.-W., and Coauthors, 2022: Radiation correction and uncertainty evaluation of RS41 temperature sensors by using an upper-air simulator. *Atmos. Meas. Tech.*, **15**, 1107–1121, https://doi.org/10.5194/amt-15-1107-2022.

Li, Q., M. Rapp, A. Schrön, A. Schneider, and G. Stober, 2016: Derivation of turbulent energy dissipation rate with the Middle Atmosphere Alomar Radar System (MAARSY) and radiosondes at Andøya, Norway. *Ann. Geophys.*, **34**, 1209–1229, https://doi.org/10.5194/angeo-34-1209-2016.

Luce, H., R. Wilson, F. Dalaudier, H. Hashiguchi, N. Nishi, Y. Shibagaki, and T. Nakajo, 2014: Simultaneous observations of tropospheric turbulence from radiosondes using Thorpe analysis and the VHF MU radar. *Radio Sci.*, **49**, 1106–1123, https://doi.org/10.1002/2013RS005355.

Lv, Y., and Coauthors, 2021: Spatiotemporal characteristics of atmospheric turbulence over China estimated using operational high-resolution soundings. *Environ. Res. Lett.*, **16**, 054050, https://doi.org/10.1088/1748-9326/abf461.

Muhsin, M., S. V. Sunilkumar, M. V. Ratnam, K. Parameswaran, B. V. K. Murthy, G. Ramkumar, and K. Rajeev, 2016: Diurnal variation of atmospheric stability and turbulence during different seasons in the troposphere and lower stratosphere derived from simultaneous radiosonde observations at two tropical stations, in the Indian Peninsula. *Atmos. Res.*, **180**, 12–23, https://doi.org/10.1016/j.atmosres.2016.04.021.

Muñoz-Esparza, D., R. D. Sharman, and S. B. Trier, 2020: On the consequences of PBL scheme diffusion on UTLS wave and turbulence representation in high-resolution NWP models. *Mon. Wea. Rev.*, **148**, 4247–4265, https://doi.org/10.1175/MWR-D-20-0102.1.

Nash, J., T. Oakley, H. Vömel, and L. I. Wei, 2011: WMO intercomparison of high quality radiosonde systems (Yangjiang, China 12 June–3 August 2010). WMO Instruments and Observing Methods Rep. 107, 248 pp., https://www.gruan.org/gruan/editor/documents/wmo/IOM-107_Yangjiang.pdf.

Nastrom, G. D., and K. S. Gage, 1985: A climatology of atmospheric wavenumber spectra of wind and temperature observed by commercial aircraft. *J. Atmos. Sci.*, **42**, 950–960, https://doi.org/10.1175/1520-0469(1985)042<0950:ACOAWS>2.0.CO;2.

Nath, D., M. Venkat Ratnam, A. K. Patra, B. V. Krishna Murthy, and S. V. Bhaskar Rao, 2010: Turbulence characteristics over tropical station Gadanki (13.5°N, 79.2°E) estimated using high-resolution GPS radiosonde data. *J. Geophys. Res.*, **115**, D07102, https://doi.org/10.1029/2009JD012347.

Osman, M. K., W. K. Hocking, and D. W. Tarasick, 2016: Parameterization of large-scale turbulent diffusion in the presence of both well-mixed and weakly mixed patchy layers. *J. Atmos. Sol.-Terr. Phys.*, **143–144**, 14–36, https://doi.org/10.1016/j.jastp.2016.02.025.

Ozmidov, R. V., 1965: On the turbulent exchange in a stably stratified ocean. *Izv. Atmos. Oceanic Phys.*, **1**, 861–871.

Pauley, P., and B. Ingleby, 2022: Assimilation of in-situ observations. *Data Assimilation for Atmospheric, Oceanic and Hydrologic Applications (Vol. IV)*, S. K. Park and L. Xu, Eds., Springer, 293–371.

Pearson, J. M., and R. D. Sharman, 2017: Prediction of energy dissipation rates for aviation turbulence. Part II: Nowcasting convective and nonconvective turbulence. *J. Appl. Meteor. Climatol.*, **56**, 339–351, https://doi.org/10.1175/JAMC-D-16-0312.1.

Pinto, J. O., and Coauthors, 2021: The status and future of small uncrewed aircraft systems (UAS) in operational meteorology. *Bull. Amer. Meteor. Soc.*, **102**, E2121–E2136, https://doi.org/10.1175/BAMS-D-20-0138.1.

Rajput, A., N. Singh, J. Singh, and S. Rastogi, 2022: Investigation of atmospheric turbulence and scale lengths using radiosonde measurements of GVAX-campaign over central Himalayan region. *J. Atmos. Sol.-Terr. Phys.*, **235**, 105895, https://doi.org/10.1016/j.jastp.2022.105895.

Rapp, M., and Coauthors, 2021: SOUTHTRAC-GW: An airborne field campaign to explore gravity wave dynamics at the world's strongest hotspot. *Bull. Amer. Meteor. Soc.*, **102**, E871–E893, https://doi.org/10.1175/BAMS-D-20-0034.1.

Schneider, A., M. Gerding, and F. J. Lübken, 2015: Comparing turbulent parameters obtained from LITOS and radiosonde measurements. *Atmos. Chem. Phys.*, **15**, 2159–2166, https://doi.org/10.5194/acp-15-2159-2015.

Scotti, A., 2015: Biases in Thorpe-scale estimates of turbulence dissipation. Part II: Energetics arguments and turbulence simulations. *J. Phys. Oceanogr.*, **45**, 2522–2543, https://doi.org/10.1175/JPO-D-14-0092.1.

Sharman, R. D., C. Tebaldi, G. Wiener, and J. Wolff, 2006: An integrated approach to mid- and upper-level turbulence forecasting. *Wea. Forecasting*, **21**, 268–287, https://doi.org/10.1175/WAF924.1.

——, and J. M. Pearson, 2017: Prediction of energy dissipation rates for aviation turbulence. Part I: Forecasting nonconvective turbulence. *J. Appl. Meteor. Climatol.*, **56**, 317–337, https://doi.org/10.1175/JAMC-D-16-0205.1.

——, L. B. Cornman, G. Meymaris, J. Pearson, and T. Farrar, 2014: Description and derived climatologies of automated in situ eddy-dissipation-rate reports of atmospheric turbulence. *J. Appl. Meteor. Climatol.*, **53**, 1416–1432, https://doi.org/10.1175/JAMC-D-13-0329.1.

Shin, H. H., and S.-Y. Hong, 2011: Intercomparison of planetary boundary-layer parametrizations in the WRF model for a single day from CASES-99. *Bound.-Layer Meteor.*, **139**, 261–281, https://doi.org/10.1007/s10546-010-9583-z.

——, W. Deierling, and R. Sharman, 2023: A comparative study of various approaches for producing probabilistic forecasts of upper-level aviation turbulence. *Wea. Forecasting*, **38**, 139–161, https://doi.org/10.1175/WAF-D-22-0086.1.

Thorpe, S. A., 1977: Turbulence and mixing in a Scottish loch. *Philos. Trans. Roy. Soc.*, **A286**, 125–181, https://doi.org/10.1098/rsta.1977.0112.

——, 2005: *The Turbulent Ocean.* Cambridge University Press, 496 pp.

Tinney, E. N., C. R. Homeyer, L. Elizalde, D. F. Hurst, A. M. Thompson, R. M. Stauffer, H. Vömel, and H. B. Selkirkh, 2022: A modern approach to a stability-based definition of the tropopause. *Mon. Wea. Rev.*, **150**, 3151–3174, https://doi.org/10.1175/MWR-D-22-0174.1.

Uppala, S. M., and Coauthors, 2005: The ERA-40 Re-Analysis. *Quart. J. Roy. Meteor. Soc.*, **131**, 2961–3012, https://doi.org/10.1256/qj.04.176.

von Rohden, C., M. Sommer, T. Naebert, V. Motuz, and R. J. Dirksen, 2022: Laboratory characterization of the radiation temperature error of radiosondes and its application to the GRUAN data processing for the Vaisala RS41. *Atmos. Meas. Tech.*, **15**, 383–405, https://doi.org/10.5194/amt-15-383-2022.

Wang, L., M. A. Geller, and D. C. Fritts, 2019: Direct numerical simulation guidance for Thorpe analysis to obtain quantitatively reliable turbulence parameters. *J. Atmos. Oceanic Technol.*, **36**, 2247–2255, https://doi.org/10.1175/JTECH-D-18-0225.1.

Wilson, R., H. Luce, F. Dalaudier, and J. Lefrère, 2010: Turbulence patch identification in potential density or temperature profiles. *J. Atmos. Oceanic Technol.*, **27**, 977–993, https://doi.org/10.1175/2010JTECHA1357.1.

——, F. Dalaudier, and H. Luce, 2011: Can one detect small-scale turbulence from standard meteorological radiosondes? *Atmos. Meas. Tech.*, **4**, 795–804, https://doi.org/10.5194/amt-4-795-2011.

——, H. Luce, H. Hashiguchi, M. Shiotani, and F. Dalaudier, 2013: On the effect of moisture on the detection of tropospheric turbulence from in situ measurements. *Atmos. Meas. Tech.*, **6**, 697–702, https://doi.org/10.5194/amt-6-697-2013.

——, H. Hashiguchi, and M. Yabuki, 2018: Vertical spectra of temperature in the free troposphere at meso-and-small scales according to the flow regime: Observations and interpretation. *Atmosphere*, **9**, 415, https://doi.org/10.3390/atmos9110415.

WMO, 1957: Definition of the tropopause. *WMO Bull.*, **6**, 136.

Woiwode, W., and Coauthors, 2023: Non-orographic gravity waves and turbulence caused by merging jet streams. *J. Geophys. Res. Atmos.*, **128**, e2022JD038097, https://doi.org/10.1029/2022JD038097.

Wolff, J. K., and R. D. Sharman, 2008: Climatology of upper-level turbulence over the contiguous United States. *J. Appl. Meteor. Climatol.*, **47**, 2198–2214, https://doi.org/10.1175/2008JAMC1799.1.

Zhang, J., S. D. Zhang, C. M. Huang, K. M. Huang, Y. Gong, Q. Gan, and Y. H. Zhang, 2019a: Latitudinal and topographical variabilities of free atmospheric turbulence from high-resolution radiosonde data sets. *J. Geophys. Res. Atmos.*, **124**, 4283–4298, https://doi.org/10.1029/2018JD029982.

——, ——, ——, ——, ——, ——, and ——, 2019b: Statistical study of atmospheric turbulence by Thorpe analysis. *J. Geophys. Res. Atmos.*, **124**, 2897–2908, https://doi.org/10.1029/2018JD029686.

——, J. Guo, S. Zhang, and J. Shao, 2022: Inertia-gravity wave energy and instability drive turbulence: Evidence from a near-global high-resolution radiosonde dataset. *Climate Dyn.*, **58**, 2927–2939, https://doi.org/10.1007/s00382-021-06075-2.